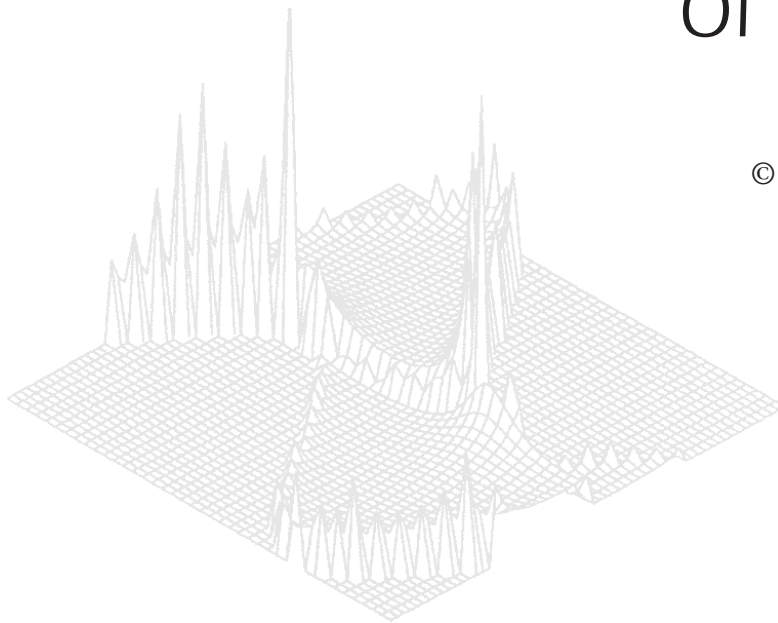

C S I R O P U B L I S H I N G

Australian Journal of Physics

Volume 52, 1999
© CSIRO Australia 1999



A journal for the publication of
original research in all branches of physics

www.publish.csiro.au/journals/ajp

All enquiries and manuscripts should be directed to

Australian Journal of Physics

CSIRO PUBLISHING

PO Box 1139 (150 Oxford St)

Collingwood

Vic. 3066

Australia

Telephone: 61 3 9662 7626

Facsimile: 61 3 9662 7611

Email: peter.robertson@publish.csiro.au



Published by **CSIRO PUBLISHING**
for CSIRO Australia and
the Australian Academy of Science



Structure and Magnetism in the Layered CMR Manganites

$\text{La}_{2-2x}\text{Sr}_{1+2x}\text{Mn}_2\text{O}_7$ ($x = 0.3, 0.4$)*

D. N. Argyriou,^{A,F} J. F. Mitchell,^B J. D. Jorgensen,^B J. B. Goodenough,^C
P. G. Radaelli,^D D. E. Cox^E and H. N. Bordallo^{A,F}

^A Los Alamos Neutron Science Center, Los Alamos National Laboratory,
Los Alamos, NM 87545, USA.

^B Materials Science Division, Argonne National Laboratory,
Argonne, IL 60439, USA.

^C Center for Material Science and Engineering, ECT 9.102,
University of Texas at Austin, Austin, TX 78712–1063, USA.

^D ISIS Facility, Rutherford Appleton Laboratory, Chilton, OX11 0QX, UK.

^E Brookhaven National Laboratory, Upton, NY 11973, USA.

^F Present address: Argonne National Laboratory, Argonne, IL 60439, USA.

Abstract

In this paper we describe a detailed neutron diffraction investigation of the crystal and magnetic structure of two layered CMR manganites $\text{La}_{1.2}\text{Sr}_{1.8}\text{Mn}_2\text{O}_7$ ($x = 0.4$) and $\text{La}_{1.4}\text{Sr}_{1.6}\text{Mn}_2\text{O}_7$ ($x = 0.3$). In these materials of reduced dimensionality compared to the 3D perovskites, we find competing effects between charge–lattice and spin degrees of freedom. These effects can be investigated by studying the behaviour of crystal and magnetic structure as a function of temperature, composition and hydrostatic pressure. We find opposite lattice responses to the onset of charge delocalisation and magnetic ordering in these two layered compounds. Below the insulator-to-metal transition (T_{IM}), the lattice response suggests that charge is transferred to $d_{3z^2-r^2}$ orbitals in $\text{La}_{1.2}\text{Sr}_{1.8}\text{Mn}_2\text{O}_7$ and to $d_{x^2-y^2}$ orbitals in $\text{La}_{1.4}\text{Sr}_{1.6}\text{Mn}_2\text{O}_7$. We argue that these changes are too large to be due to chemical differences. Instead we suggest that the orbital configuration of the Mn ion below T_{IM} is sensitive to electronic doping. In $\text{La}_{1.2}\text{Sr}_{1.8}\text{Mn}_2\text{O}_7$ we find that the lattice response at T_{IM} to be driven by lattice displacements that relax below T_{IM} , consistent with polaronic degrees of freedom. We also note that the competition between super- and double-exchange to be significant in reduced dimensions. This is manifested in the change in the sign of the apical Mn–O bond compressibilities above and below T_{IM} . Finally, we describe the magnetic structure of these two different layered manganites. We find that electronic doping also results in significant changes to the ordered arrangement of Mn spins. Interestingly the magnetism in reduced dimensions in these materials can be varied from relative simple structures that show ferromagnetic inter-bilayer coupling as observed in $\text{La}_{1.2}\text{Sr}_{1.8}\text{Mn}_2\text{O}_7$ to structures with antiferromagnetic inter-bilayer coupling as found in $\text{La}_{1.4}\text{Sr}_{1.6}\text{Mn}_2\text{O}_7$.

1. Introduction

The strong coupling between magnetism and charge transport in the manganite perovskites has been known since the 1950s (Jonker and Staten 1950; Wollen and Koehler). However, their recent rediscovery has centred on the observation of new phenomena such magnetotransport (Hwang *et al.* 1995) and magnetostructural effects (Radaelli *et al.* 1995) that highlight the interplay between spin, charge and

* Refereed paper based on a contribution to the International Workshop on the Colossal Magnetoresistance (CMR) Effect, held at the University of Melbourne, 8–11 June 1998.

lattice degrees of freedom in these materials. While the work on CMR materials has concentrated on the 3D perovskite manganites, the discovery of the layered compound $\text{La}_{2-2x}\text{Sr}_{1+2x}\text{Mn}_2\text{O}_7$ (Moritomo *et al.* 1996) presents another class of CMR oxides. These naturally layered manganites provide a rich opportunity to not only investigate the interplay between spin, charge and lattice in reduced dimensions, but also to explore novel new phenomena that are not found in the 3D perovskite manganites.

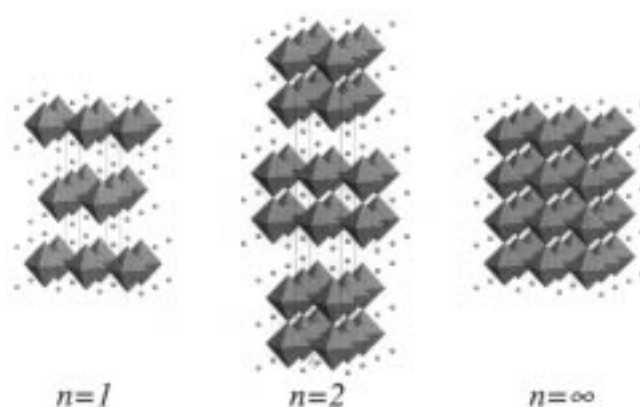


Fig. 1. The $(\text{La}, \text{Sr})_{n+1}\text{Mn}_n\text{O}_{3n+1}$ series. For $n = 1$ a single perovskite layer is formed separated by a $(\text{La}, \text{Sr})\text{O}$ rocksalt layer, while for $n = 2$ a perovskite bilayer is formed. For $n = \infty$ the perovskite structure results.

Moritomo *et al.* (1996) originally investigated the effect of reduced dimensionality on the CMR effect in the manganites by synthesising the Ruddlesden–Popper series of compounds, $(\text{La}, \text{Sr})_{n+1}\text{Mn}_n\text{O}_{3n+1}$, shown in Fig. 1 (in this series $n = \infty$ corresponds to the perovskite structure). These studies demonstrated that the perovskite bilayer compound $\text{La}_{1.2}\text{Sr}_{1.8}\text{Mn}_2\text{O}_7$ ($x = 0.4$) exhibits a coupled insulator–metal (IM) and a paramagnetic to ferromagnetic transition at $T_{\text{IM}} = 120$ K, while the single layered materials $\text{La}_{1.2}\text{Sr}_{0.8}\text{MnO}_4$ remain insulating even at lower temperatures. An important effect of the lower dimensionality of these materials is the enhanced CMR compared to perovskite materials especially at low field, $\sim 200\%$ at 129 K in 0.3 T (Moritomo *et al.* 1996). Similar CMR values are obtained in perovskite manganites in much higher applied fields, 7–9 T (Hwang *et al.* 1995). The possibility of technological applications using these layered manganites has contributed to the considerable progress in understanding the physical properties of the $\text{La}_{2-2x}\text{Sr}_{1+2x}\text{Mn}_2\text{O}_7$ system. (In this notation x not only describes the nominal chemical doping but also the nominal electronic doping.)

The structure of the $n = 2$ layered manganite $\text{La}_{2-2x}\text{Sr}_{1+2x}\text{Mn}_2\text{O}_7$ is shown in Fig. 1. Here the 3D network of MnO_6 octahedra found in the perovskite structure is interrupted by a $(\text{La}, \text{Sr})\text{O}$ rock salt layer to form alternating stacking of perovskite $(\text{La}, \text{Sr})\text{MnO}_3$ bilayers and $(\text{La}, \text{Sr})\text{O}$ layers. This stacking allows for extra degrees of freedom of the MnO_6 octahedron not found in the perovskite manganites. This is demonstrated by the three crystallographically different

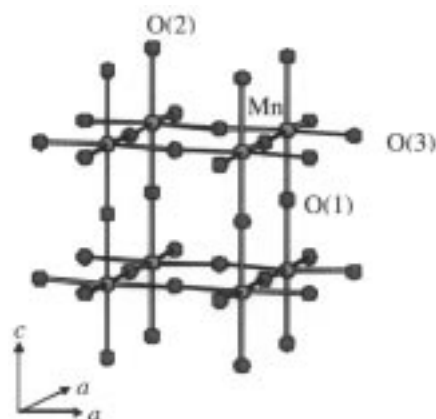


Fig. 2. A single perovskite bilayer in the Ruddlesden–Popper $n = 2$ phase. The positions of the three oxygen sites are shown, as well as the Mn site. The La, Sr sites are omitted for clarity.

oxygen sites that make up the MnO_6 octahedron: (a) the O(1) oxygen which is bonded to two other Mn atoms and is located between the MnO_2 sheets (see Fig. 2 for a detailed view of the perovskite bilayer and atom labeling); (b) the O(2) oxygen that is bonded to only one Mn atom and it is ionically coordinated to La, Sr sites within the rock-salt layered; and (c) the O(3) oxygen that forms MnO_2 sheets along the ab -plane. In early studies of the structure–property relationships in the CMR perovskites much attention was focused on the Mn–O–Mn bond angle as it is considered to be a critical parameter relevant to the one-electron bandwidth of these materials (Fontcuberta *et al.* 1996). Attention on the Mn–O–Mn angle stems from earlier work in the nickelate perovskites where the Ni–O–Ni bond angle can be tuned to drive these materials from an insulator to a metal at low temperatures (Torrence *et al.* 1992). In the case of the layered manganites we find that the Mn–O(3)–Mn angle is almost straight at 178° , while the Mn–O(1)–Mn angle along the c -axis is set by symmetry to 180° . The small buckling of the Mn–O(3)–Mn angle implies a substantial one-electron bandwidth parallel to the infinite MnO_2 layers. On the other hand, conductivity along the c -axis is more likely via a tunneling mechanism through the (La, Sr)O insulating layer. Indeed, Moritomo *et al.* (1996) have shown that the c -axis resistivity is two orders of magnitude larger than the in-plane resistivity. We have found that the Mn–O(3)–Mn angle bond angle does not vary significantly as a function of temperature or composition between $x = 0.3$ – 0.4 or as a function of pressure up to 6 kbar (Mitchell *et al.* 1997; Argyriou *et al.* 1997a, 1997b). Rather, changes in the Mn–O bonds themselves are far more critical parameters to charge delocalisation and magnetism as we shall see below.

Enough information has emerged to form a more detailed picture of the electronic and magnetic phase diagram of the $\text{La}_{2-2x}\text{Sr}_{1+2x}\text{Mn}_2\text{O}_7$ system since the original work of Moritomo *et al.* (1996). Indeed recently Mitchell *et al.* (1998) have highlighted the rich magnetic phase diagram that can be obtained in this system between the compositional range $0.3 < x < 0.5$ as shown in Fig. 3. For $x = 0.5$ it is found that Mn spins lie within the ab -plane but form an insulating antiferromagnetic arrangement resulting in a type A antiferromagnetic structure within a perovskite bilayer (Battle *et al.* 1996). Very recently evidence of a charge ordered state has been reported for this composition (Kimura *et al.*

1998). With decreasing doping at $x = 0.4$ a simple ferromagnetic structure is observed with Mn spins ferromagnetically aligned within the ab -plane (Mitchell *et al.* 1997). Within this region ferromagnetism is accompanied with charge delocalisation (Moritomo *et al.* 1996; Mitchell *et al.* 1997). Below $x = 0.35$, neutron diffraction measurements observe a change of the easy axis from the ab -plane to along the c -axis (Mitchell *et al.* 1998). Further decrease of the nominal doping to $x = 0.3$ results in an antiferromagnetic state built by ferromagnetic perovskite bilayers that are antiferromagnetically coupled (Argyriou *et al.* 1998). For this composition Kimura *et al.* (1996, 1997) have recently reported the observation of spin-polarised inter-layer conductivity and high CMR (10% at 50 kOe and at 90 K).

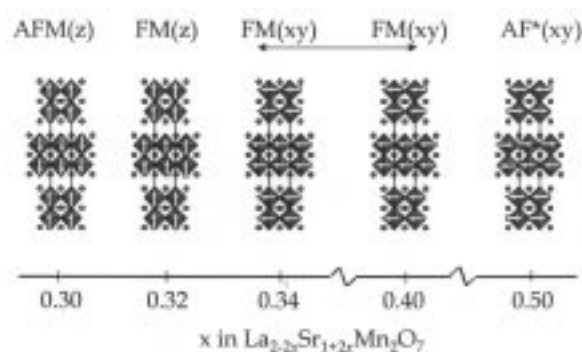


Fig. 3. Doping dependence of the 20 K magnetic structure of the $\text{La}_{2-2x}\text{Sr}_{1+2x}\text{Mn}_2\text{O}_7$ series as determined by neutron powder diffraction.

Discussions on the physical origin of colossal magnetoresistance (CMR) in the manganite perovskites originally focused on the double exchange (DE) of e_g carriers between ferromagnetically coupled Mn^{3+} and Mn^{4+} ions (Zener 1951). However, recent theoretical work demonstrated that the DE model alone does not explain quantitatively the CMR effect in $\text{La}_{1-x}\text{M}_x\text{MnO}_3$ (Millis *et al.* 1995; Roder *et al.* 1996). Rather, it is suggested that a strong electron–phonon coupling arising from the local Jahn–Teller (JT) distortions of Mn^{3+} ions due to the slow hopping of e_g carriers may explain the magnetotransport and magnetostructural phenomena observed in these materials. A more coherent picture for the lattice polaron formation associated with the insulator–metal transition in the manganites has emerged (Zhao *et al.* 1996). It has become increasingly evident that the correlation between local structural changes and polaron formation can provide an adequate description for the anomalies observed in many experiments, such as the unusual temperature dependence of Debye–Waller factors and lattice parameters (Radaelli *et al.* 1995, 1996), large frequency shifts of the internal infrared modes (Kim *et al.* 1996), variations in the local structure as seen by pair distribution function (PDF) analysis (Billinge *et al.* 1996) and EXAFS (Booth *et al.* 1998).

Magnetic interactions in the manganites have been described in terms of super- and double-exchange and the competition between them. These interactions involve the antiferromagnetic $t^3-p_\pi-t^3$ π -bonding component between half-filled t_{2g} orbitals of the high-spin Mn^{3+} or Mn^{4+} configurations and the ferromagnetic

$e^1-p_\sigma-e^0$ component that dominates the σ -bonding interactions via electrons in the twofold-degenerate states of e_g orbital parentage (Goodenough 1972). Both interactions involve a charge transfer that preserves the spin angular momentum. The t^3 configurations remain localised, so transfer of a t electron to create a t^4 configuration at a neighbouring Mn atom requires an energy U_π and is constrained by the Pauli exclusion principle to have a component of the transferred electron spin antiparallel to the spin of the t^3 configuration at the acceptor Mn atom. This antiferromagnetic $t^3-p_\pi-t^3$ superexchange interaction is described by second-order perturbation theory; it gives a stabilisation energy, $\epsilon_t^s \sim -b_\pi^2 \sin^2(\theta/2)/U_\pi \sim b_\pi^2 \cos\theta/U_\pi$, where b_π is the spin-independent transfer-energy matrix element and θ is the angle between spins at neighbouring Mn atoms along the c -axis. A value of $\theta = \pi$ gives an attractive Mn–O–Mn interaction, while $\theta = 0$ gives a repulsive interaction. The $e^1-p_\sigma-e^0$ interaction, on the other hand, involves transfer of an e electron to an empty e orbital; this transfer is not constrained by the Pauli exclusion principle, but a strong ferromagnetic intra-atomic exchange favours transfer to an acceptor having its spin ferromagnetically aligned with respect to that of the transferred electron. This ferromagnetic $e^1-p_\sigma-e^0$ interaction is stronger than the $t^3-p_\pi-t^3$ interaction whether the charge transfer is virtual (super-exchange) or real (double-exchange).

An additional parameter in considering the relationship between magnetic structure, crystal structure and electronic conductivity is the orbital degrees of freedom. This is clearly demonstrated recently by the observation of type-A antiferromagnetism and metallic conductivity in $\text{La}_{0.46}\text{Sr}_{0.54}\text{MnO}_3$ by Akimoto *et al.* (1998). They have suggested that quasi-2D metallic conductivity in $\text{La}_{0.46}\text{Sr}_{0.54}\text{MnO}_3$ occurs in the planes via double exchange in $d_{x^2-y^2}$ bands, while super-exchange dominates along the z -axis. This may be possible due to a high anisotropy between $d_{x^2-y^2}$ and $d_{3z^2-r^2}$ orbitals found in this perovskite manganite.

In this paper we present detailed crystal and magnetic structure results using neutron diffraction for two compositions, $\text{La}_{1.2}\text{Sr}_{1.8}\text{Mn}_2\text{O}_7$ ($x = 0.4$) and $\text{La}_{1.4}\text{Sr}_{1.6}\text{Mn}_2\text{O}_7$ ($x = 0.3$). This work highlights not only the spin–charge–lattice coupling in reduced dimensions but also the sensitivity of the spin and orbital degrees of freedom to electronic doping. We describe the response of the lattice to charge delocalisation and magnetic ordering which is opposite in these two layered CMR compounds. We argue that these changes are too large to be ascribed to the variation in the size of the A-size cation. Rather we suggest that electronic doping directly affects the orbital degrees of freedom of the Mn ion below T_{IM} . In $\text{La}_{1.2}\text{Sr}_{1.8}\text{Mn}_2\text{O}_7$ we find that the lattice response at T_{IM} to be driven by lattice displacements that relax below T_{IM} , consistent with polaronic degrees of freedom. Our measurements also demonstrate that the competition between super- and double-exchange that has been well described in the 3D perovskite manganites to be also significant in reduced dimensions. This is manifested in the change in the sign of the apical Mn–O bond compressibilities above and below T_{IM} . Finally we describe the magnetic structure of these two different layered manganites. We find that electronic doping also results in significant change in the ordered arrangement of Mn spins. Interestingly the magnetism in reduced dimensions in these materials can be varied from relative simple structures that show ferromagnetic inter-bilayer coupling as observed in

$\text{La}_{1.2}\text{Sr}_{1.8}\text{Mn}_2\text{O}_7$ to structures with antiferromagnetic inter-bilayer coupling as found in $\text{La}_{1.4}\text{Sr}_{1.6}\text{Mn}_2\text{O}_7$.

2. Experimental

Single crystals of $\text{La}_{2-2x}\text{Sr}_{1+2x}\text{Mn}_2\text{O}_7$ ($x = 0.3, 0.4$) were melt-grown in flowing 100% O_2 in a floating zone optical image furnace (NEC SC-M15HD). Crystals were characterised using inductively coupled plasma (ICP) analysis, yielding an *average* composition of $x = 0.30(1)$ and $x = 0.40(1)$ respectively. Transport measurements on small specimens from these crystal boules have been reported elsewhere (Mitchell *et al.* 1997; Li *et al.* 1998). For the $x = 0.4$ sample an insulator–metal-like transition was observed at 120 K, and at 100 K for the $x = 0.3$ sample.

The crystal and magnetic structure of these materials was investigated using powder neutron diffraction from crystalline samples of pulverised boules. Powder data were measured using the Special Environment Powder Diffractometer (SEPD) at Argonne's Intense Pulsed Neutron Source between 20 and 505 K for $\text{La}_{1.2}\text{Sr}_{1.8}\text{Mn}_2\text{O}_7$ and between 20 and 300 K for $\text{La}_{1.4}\text{Sr}_{1.6}\text{Mn}_2\text{O}_7$. Additional neutron powder diffraction data to determine the magnetic structure of the $\text{La}_{1.4}\text{Sr}_{1.6}\text{Mn}_2\text{O}_7$ sample were measured on the high flux diffractometer D20 operated at the Institut Laue–Langevin ($\lambda = 2.41 \text{ \AA}$, $2\theta = 0\text{--}160^\circ$) between 5–150 K. Powder neutron diffraction data were analysed using the Rietveld method and the program GSAS. Refinement of the layered $\text{La}_{2-2x}\text{Sr}_{1+2x}\text{Mn}_2\text{O}_7$ phase was carried out in the space group $I4/mmm$ for all temperatures for both $x = 0.3$ and $x = 0.4$ samples. Typically, impurity phases identified as $(\text{La}, \text{Sr})_2\text{MnO}_4$ and $(\text{La}, \text{Sr})\text{MnO}_3$ were included in the refinements (Mitchell *et al.* 1997). These impurities make up approximately 5% of the pulverised powder sample.

The quality (chemical phase homogeneity) of the $\text{La}_{1.4}\text{Sr}_{1.6}\text{Mn}_2\text{O}_7$ powdered crystalline sample was investigated as a function of temperature (20–300 K) using high resolution X-ray diffraction, performed at beam line X7A at the National Synchrotron Light Source (NSLS) at the Brookhaven National Laboratory, using a wavelength of 0.8 \AA and a Ge(111)/Ge(220) monochromator/analyser combination.

3. The Manganite $\text{La}_{1.2}\text{Sr}_{1.8}\text{Mn}_2\text{O}_7$

(3a) Lattice Effects in Ferromagnetic $\text{La}_{1.2}\text{Sr}_{1.8}\text{Mn}_2\text{O}_7$

The magnetic and transport behaviour of our $\text{La}_{1.2}\text{Sr}_{1.8}\text{Mn}_2\text{O}_7$ sample as a function of temperature is shown in Fig. 4. A sharp transition is observed in both measurements at 120 K, signalling the onset of ferromagnetic order and an associated insulator–metal transition (Mitchell *et al.* 1997). These coincident magnetic and electronic transitions are common in perovskite CMR materials and have both been observed by Moritomo *et al.* (1996) in their single crystal study of $\text{La}_{1.2}\text{Sr}_{1.8}\text{Mn}_2\text{O}_7$.

Like the manganite perovskites, we found substantial lattice effects associated with the electronic and magnetic transition for $\text{La}_{1.2}\text{Sr}_{1.8}\text{Mn}_2\text{O}_7$. Fig. 5 shows the evolution with temperature of the unit cell volume and the tetragonal lattice parameters. While these lattice effects occur over a narrow temperature range, our data suggest a continuous phase transition. The unit cell volume decreases

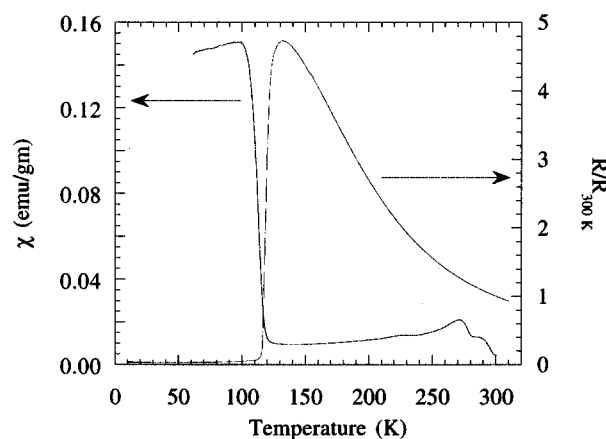


Fig. 4. The ac susceptibility ($H = 0.1$ Oe; 100 Hz) and resistance normalised to $R(300\text{ K})$ versus temperature for $\text{La}_{1.2}\text{Sr}_{1.8}\text{Mn}_2\text{O}_7$.

monotonically with decreasing temperature with a change in slope at T_{IM} . The volume decreases by $\sim 0.1\%$ through the transition. A similar behaviour has been reported for the perovskite $\text{La}_{0.75}\text{Ca}_{0.25}\text{MnO}_3$ by Radaelli *et al.* (1995). Similar to the perovskites, the unit cell axes change over a narrow temperature range near T_{IM} ; the c axis expands by $\sim 0.06\%$ and the a axis contracts by $\sim 0.16\%$. However, for $T > T_{\text{IM}}$, the a axis behaves quite differently to the c axis. Between 500 and 120 K the c axis contracts linearly with temperature, decreasing by 0.71% . From 500 to 300 K, the a axis contracts linearly with decreasing temperature by $\sim 0.14\%$. However, at $T \sim 280\text{--}300$ K, the thermal expansion of the a axis begins to deviate from linearity. Between 280 K and T_{IM} , the a axis shrinks only an additional 0.03% before rapidly contracting beginning at T_{IM} .

The temperature evolution of the three symmetry-independent Mn–O bond lengths suggests that the relationship between the JT distortion and electronic transport in the layered materials may be quite different to that observed in the perovskites. Caignaert *et al.* (1995) have recently shown that the JT distortion coordinate $D = d_{\text{Mn-O(apical)}}/d_{\text{Mn-O(equatorial)}}$ in $\text{Pr}_{0.7}\text{Ca}_{0.2}\text{Sr}_{0.1}\text{MnO}_3$ increases with decreasing temperature and then dramatically plummets at the metal–insulator transition. Such behaviour indicates that in the perovskite the itinerant electronic state is characterised by a less distorted MnO_6 octahedron than the localised state. Radaelli *et al.* (1996) have reported a similar effect in $\text{La}_{0.35}\text{Pr}_{0.35}\text{Ca}_{0.3}\text{MnO}_3$. Fig. 6 shows the evolution of D with temperature in the two-dimensional $\text{La}_{1.2}\text{Sr}_{1.8}\text{Mn}_2\text{O}_7$. Here we have taken the average of Mn–O(1) and Mn–O(2) for $d_{\text{Mn-O(apical)}}$. In contrast to the perovskites mentioned above, D slowly decreases with decreasing temperature until the onset of ferromagnetism at 120 K—and its attendant metal–insulator transition—where D sharply *increases* by $\sim 0.6\%$. Thus the delocalisation of charge is accompanied by an increase in the distortion of the MnO_6 octahedron, a distinct contrast with the perovskites. Fig. 7 gives a more detailed picture of the Mn–O bond lengths as a function

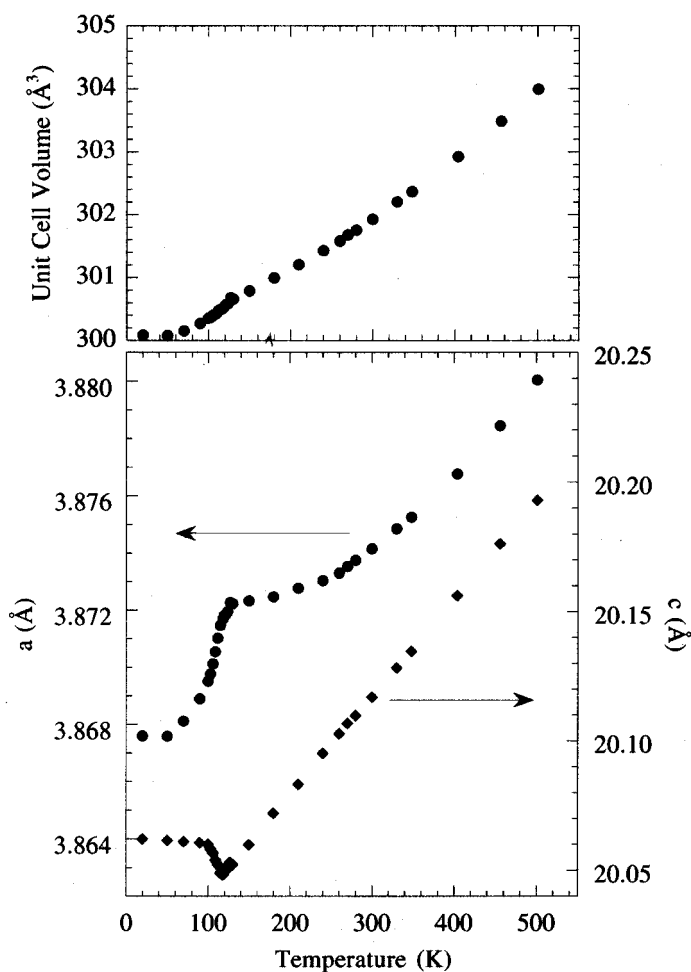


Fig. 5. Unit cell volume (upper panel) and lattice parameters (lower panel) versus temperature in $\text{La}_{1.2}\text{Sr}_{1.8}\text{Mn}_2\text{O}_7$. Error bars are smaller than the symbols.

of temperature. In particular, they show that the equatorial Mn–O(3) bond tracks the a axis, contracting at the insulator-to-metal transition by $\sim 0.14\%$. Archibald *et al.* (1996) and Goodenough (1972) have suggested that such a contraction results from the localised Mn–O antibonding e_g electron becoming itinerant; the loss of anti-bonding electron density in the Mn–O bond results in its contraction. The apical bond to the oxygen lying between the two MnO_2 layers, Mn–O(1), is only weakly temperature dependent. In fact, five bonds (four equatorial, one apical) are quite similar for all temperatures measured and are essentially identical at 20 K. It is the apical Mn–O(2) bond with its unshared oxygen atom that is longer than the other five bonds at all temperatures and that expands even more through the magnetic transition. The apical Mn–O(2) bond reaches a minimum at T_c and then increases from $1.984(4)$ to $2.002(4)$ Å ($\sim 0.91\%$) at temperatures immediately below T_c . The increased Mn–O(2) bond

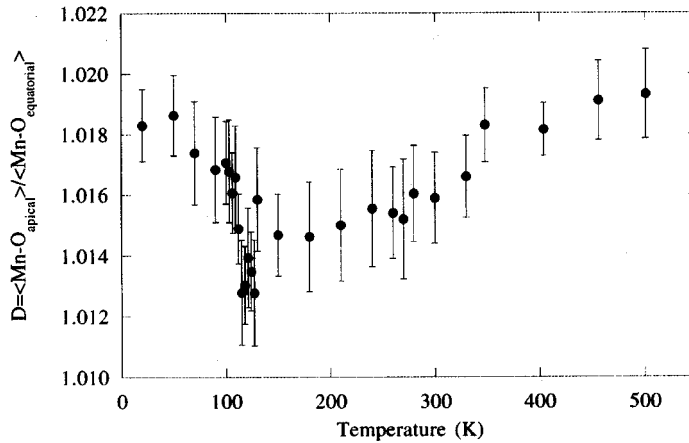


Fig. 6. Octahedral distortion, $D = \text{Mn-O}_{\text{apical}}/\text{Mn-O}_{\text{equatorial}}$ versus temperature for $\text{La}_{1.2}\text{Sr}_{1.8}\text{Mn}_2\text{O}_7$.

suggests that this response may be due to charge transfer from $d_{x^2-y^2}$ orbitals to $d_{3z^2-r^2}$ orbitals as suggested above.

(3b) Lattice Distortions in $\text{La}_{1.2}\text{Sr}_{1.8}\text{Mn}_2\text{O}_7$

The anomalies seen in the temperature dependence of the lattice parameters in $\text{La}_{1.2}\text{Sr}_{1.8}\text{Mn}_2\text{O}_7$ both at T_c and the deviation from expected thermal expansion at ~ 300 K correlates with anomalies in the temperature dependence of the displacement parameters (Debye–Waller factors) for the Mn and O atoms. In Fig. 8 we show the temperature dependence of the displacement parameters for the three oxygen and Mn atoms, as well as the temperature dependence of the three Mn–O bonds, as determined from the Rietveld analysis of powder diffraction data reported elsewhere (Mitchell *et al.* 1997). Accompanying the significant changes in the Mn–O bond lengths as discussed above there are also notable changes in the displacement parameters for the Mn and O atoms. We find that the Mn displacement parameters shows a linear behaviour above 300 K, and then saturate to a constant value between T_{IM} and 300 K. This behaviour is similar to that observed for the Mn–O(3) bond length. At T_{IM} the displacement parameters for both the Mn and O(3) atoms show an abrupt decrease [$\Delta U_{T_{\text{IM}}} \sim 0.0016 \text{ \AA}^2$ for O(3) and 0.001 \AA^2 for the Mn atom] accompanying the contraction of the Mn–O(3) bond. A smaller decrease of the displacement parameter is seen for the apical O(2) oxygen, despite the significant expansion of the Mn–O(2) at T_{IM} , while no significant anomaly is observed for either the Mn–O(1) bond or the O(1) displacement parameter.

These measurements suggest that the coupled electronic and magnetic transitions in these layered manganites are accompanied by a structural transition from a state with a broad distribution of Mn–O bond lengths above T_{IM} , to a state characterised by a sharper Mn–O bond length distribution. Thus, our observation of anomalous behaviour of the displacement parameters supports the notion of the slow hopping of the e_g carrier and the associated JT distortion of Mn^{3+} (and relaxation to Mn^{4+}) in the lattice as proposed by Millis *et al.* (1995)

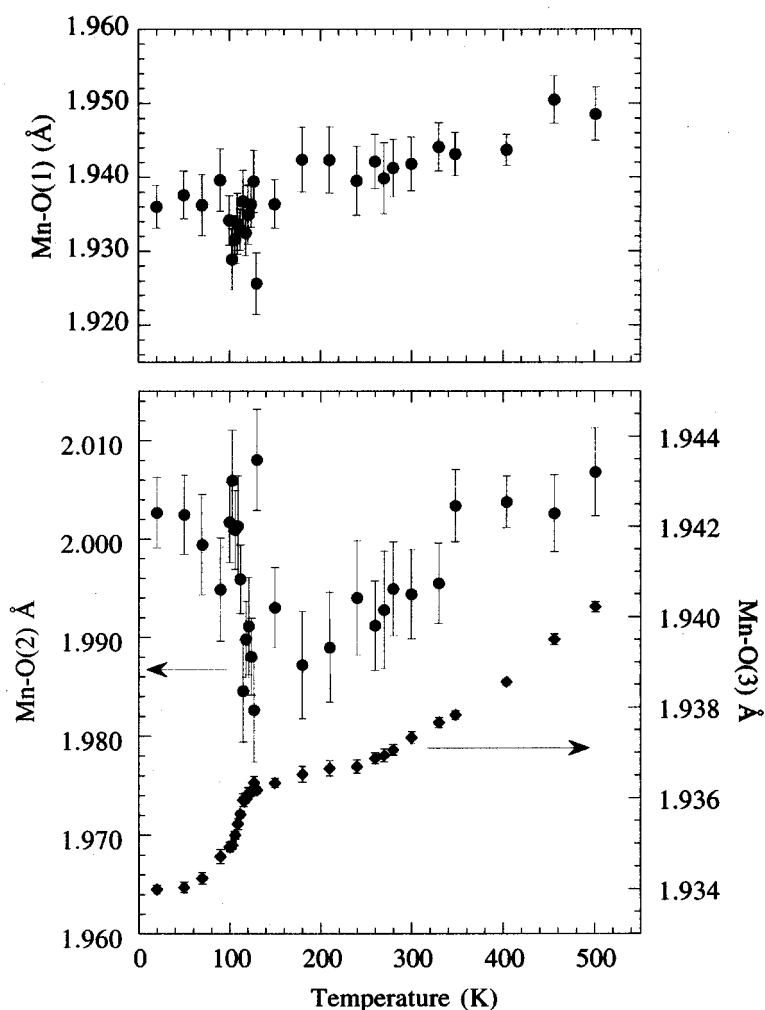


Fig. 7. Mn–O bond lengths versus temperature.

and Roder *et al.* (1996). In this context the displacement parameter data indicate a build up of lattice displacements above T_{IM} . The amplitude of these displacements effectively result in an increase of the average Mn–O(3) bond as measured by conventional crystallographic analysis, while their temperature dependence as well as theoretical considerations suggest that they are dynamic in nature. The onset of the delocalisation of e_g carriers results in a decrease in the amplitude of these displacement parameters and consequently to a decrease of the average Mn–O(3) bond and increase of the average Mn–O(2) bond as described above.

(3c) Magnetism in $La_{1.2}Sr_{1.8}Mn_2O_7$

Below T_c , magnetic reflections reveal that the Mn spins lie entirely within the ab -plane (see Fig. 2). That is, this two-dimensional system exhibits no spin canting along the c axis such as that observed in the three-dimensional

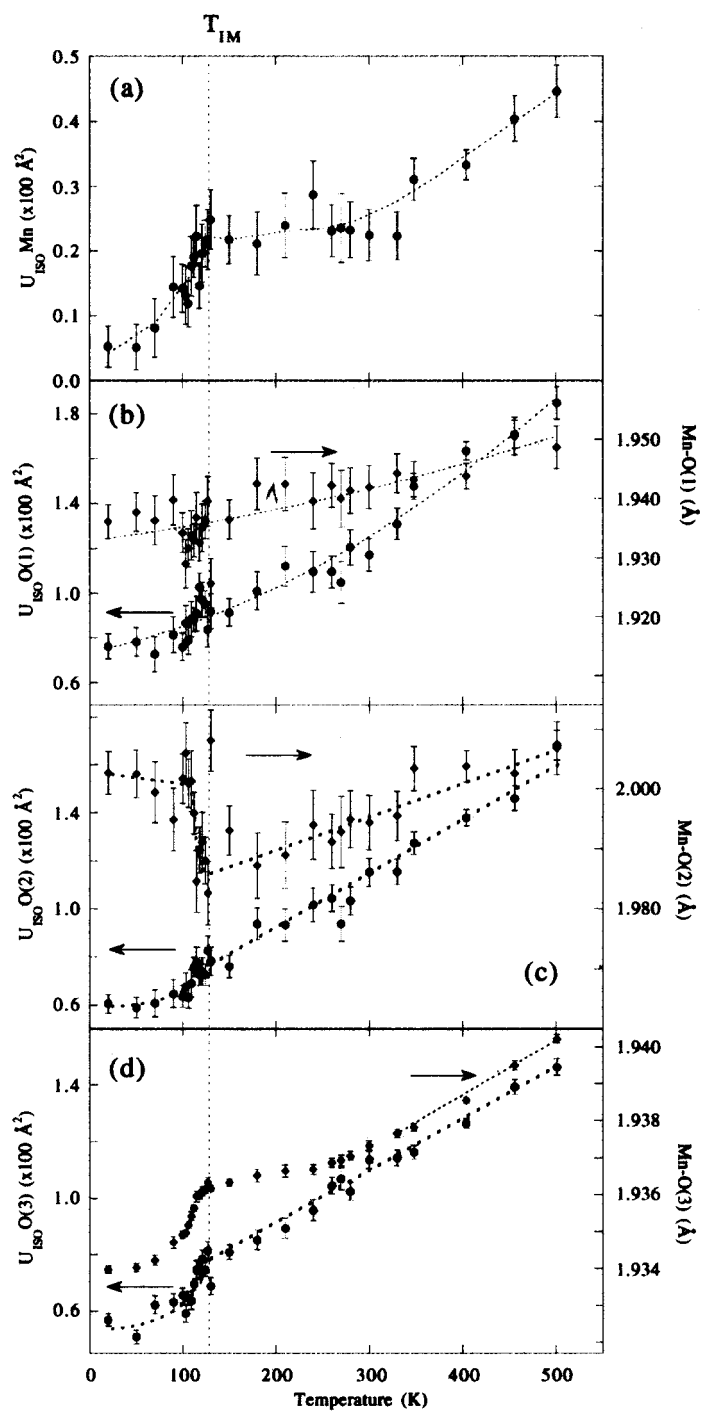


Fig. 8. Isotropic displacement parameters for the (a) Mn, (b) O(1), (c) O(2) and (d) O(3) atoms as a function of temperature. The temperature dependence of the Mn-O bond length is also shown.

(La, Sr)MnO₃ perovskite system. The saturation moment obtained from our Rietveld refinement is $3.0(1) \mu_B/\text{Mn}$ at 20 K, consistent with Moritomo's magnetisation data showing the easy axis lying in the MnO₂ plane and a $3 \mu_B/\text{Mn}$ saturation magnetisation at 120 K with $H = 5.5 \text{ T}$.

However, spin canting between adjacent MnO₂ sheets may exist below T_c . This conclusion arises from compressibility measurements of La_{1.2}Sr_{1.8}Mn₂O₇ above and below T_c . Here powder neutron diffraction data were measured from the same sample used in the studies described above, as a function of pressure between 0–6.5 kbar at 100, 200 and 300 K (Argyriou *et al.* 1997*b*). Data were analysed using the Rietveld method to obtain crystal and magnetic structure information. The refinements at 100 K, below T_c , indicated that there was no spin rotation out of the *ab*-plane as a function of pressure. Neither was there any evidence of a pressure induced structural transition at any pressure or temperature.

A linear fit to the refined lattice parameters as a function of pressure measured at 300, 200 and 100 K was used to compute the compressibility of La_{1.2}Sr_{1.8}Mn₂O₇ at these temperatures (see Fig. 9). The *a*-axis compressibilities remain almost constant with temperature, while the *c*-axis compressibility becomes more positive (less compressible) with decreasing temperature. The combination of the

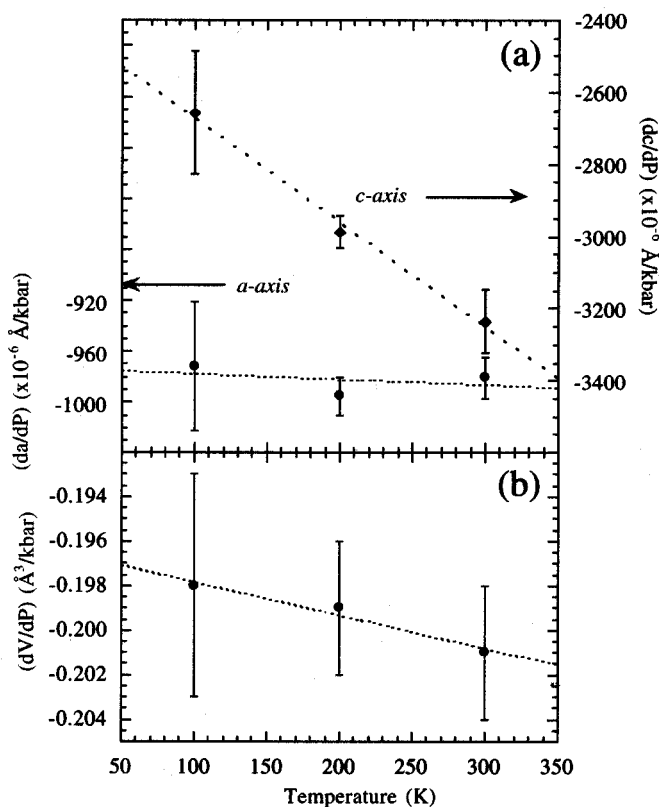


Fig. 9. Compressibilities of the *a*- and *c*-axis (upper panel) and unit cell volume (lower panel) versus temperature.

a - and c -axis compressibility thus results in a volume compressibility that increases slightly with decreasing temperature. The a -axis compressibility is accounted for wholly by the reduction of the Mn–O(3) bond length (-0.15% over 6 kbar) (see Figs 10c and 10f) for all temperatures examined; the Mn–O(3)–Mn bond angle remains unchanged within experimental error at $178.6(4)^\circ$, indicating no additional buckling of MnO_6 octahedra occurs with applied pressure. This is in contrast to other perovskite materials (Jorgensen *et al.* 1986; Zhao *et al.* 1993), where application of pressure results primarily in a tilting of the MnO_6 octahedra, rather than changes of the Mn–O bond lengths.

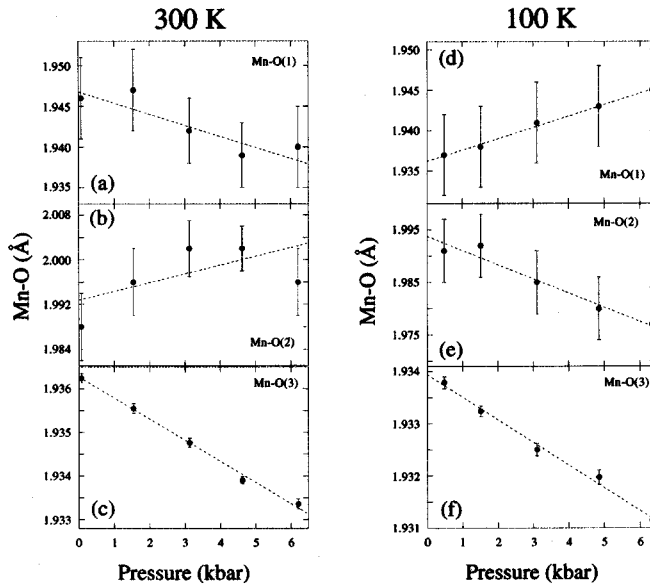


Fig. 10. Variation of Mn–O bond lengths in $\text{La}_{1.2}\text{Sr}_{1.8}\text{Mn}_2\text{O}_7$ with pressure at 300 K (*left*) and 100 K (*right*). Dashed lines are weighted least square fits to the data.

Although the c -axis compressibility changes linearly with temperature, investigation of the compressibilities of the individual c -axis Mn–O bonds reveals two remarkable findings: (1) the pressure variations of distinguishable Mn–O(1) and Mn–O(2) bond lengths have opposite signs and (2) the signs of these variations are opposite in the PI regime at 300 K (see Figs 10a and 10b) to what they are in the FM state at 100 K (see Figs 10d and 10e). The compressibilities of the individual Mn–O apical bonds bear no relation to the overall c -axis compressibility, but their sum does vary consistently and is accommodated by the relaxation of the remainder of the lattice. That the O(1) and O(2) oxygen atoms share the same Mn $d_{3z^2-r^2}$ orbital while exhibiting opposite Mn–O compressibilities forces consideration of the Mn–O(1)–Mn interactions in contrast to the Mn–O(2)–(La, Sr) interactions.

The response of the individual Mn–O bond lengths to applied pressure in the PI and FM states reflects a change in the c -axis Mn–O–Mn interactions with the degree of ferromagnetic alignment of pairs of ferromagnetic MnO_2 sheets.

The observed compressibilities are consistent with a magnetic structure in which the ferromagnetic MnO_2 sheets have magnetisations canted with respect to one another. In the FM state, the charge transfer between and within MnO_2 planes is real, and optimisation of θ for the sum of the super-exchange and double-exchange components gives a cant angle θ_0 of $\cos(\theta_0/2) \sim b_\sigma U_\pi / b^2 < 1$. A value of $\theta_0 = 0$ is stabilised below T_c *within* ferromagnetic MnO_2 planes, but the compressibility data imply a value of $\cos(\theta_0/2) < 1$ for the magnetic coupling *between* planes. Since b_σ contains a larger Mn–O overlap integral than b_π , the pressure increases as $\cos(\theta_0/2)$, thereby reducing the angle θ_0 and increasing the $t^3 - p_\pi - t^3$ spin–spin repulsion between MnO_2 planes. A change in lattice parameters induced by changes in bonding as a result of magnetic order represents an *exchange striction*; a phenomenon common to magnetic oxides (Goodenough 1963, 1972).

In $\text{La}_{1.2}\text{Sr}_{1.8}\text{Mn}_2\text{O}_7$, each Mn atom sees an Mn–O–Mn interaction on only one side along the c -axis; the Mn–O–(La, Sr) interaction contains a Mn–O bond length that is free to adjust to that on the Mn–O–Mn side so as to retain the mean Mn–O bond length characteristic of the valence-bond sum, which is why the c -axis Mn–O bonds on opposite sides of a Mn atom vary reciprocally with temperature and pressure. In the absence of magnetic order in the PI state, there is no spin–spin repulsion and pressure increases the overlap integrals in both b_π and b_σ to give a normal reduction of the equilibrium Mn–O bond lengths within and between the MnO_2 sheets. This behaviour is clearly seen for the Mn–O(1) and Mn–O(3) bonds at 300 K (see Fig. 3). The Mn–O(2) bond length behaves differently because it is not part of the Mn–O–Mn linkage (see Figs 1 and 2); it responds to the Mn–O(1) and Mn–O(3) bond length changes so as to conserve the mean equilibrium bond-length sum for the Mn valences. We have omitted from this qualitative discussion the influence of any redistribution of electrons between $d_{x^2-y^2}$ and $d_{3z^2-r^2}$ orbitals with pressure, as such a redistribution would not contribute to a sign reversal of the Mn–O(1) and Mn–O(2) compressibilities on crossing T_c .

In the absence of magnetic superlattice reflections, the neutron powder diffraction data are consistent with the type-A canted spin ferromagnetic model proposed. They indicate a ferromagnetic coupling within MnO_2 basal planes below T_c . Analysis of the diffraction data using models with a z -component of the spin parallel to the c -axis consistently produces values of $\mu_z = 0$ at all pressures examined. Because of the tetragonal symmetry of the lattice, single-crystal neutron-diffraction studies are needed to confirm whether there is the predicted cant angle in the ab -planes between spins of neighbouring MnO_2 planes. However, an observed increase in the Mn moment from 2.5 to 2.8 μ_B over 6 kbar of pressure is consistent with the predicted decrease of cant angle θ_0 and a positive dT_c/dP for this compound (see Fig. 11).

In conclusion, the surprising reversal in the sign of the Mn–O(1) bond compressibility on passing from the PI to the FM state can be interpreted as a manifestation of exchange striction; a cant angle θ_0 between the magnetisations of the pairs of MnO_2 sheets within a perovskite layer is predicted for this layered manganite. Very recently such a spin canted structure has been observed in single crystal neutron measurements by Hirota *et al.* (1998). Further investigation of the spin fluctuation spectrum above T_c has shown that it is dominated by spin canting with perovskite bilayers as described above (Osborn *et al.* 1998).

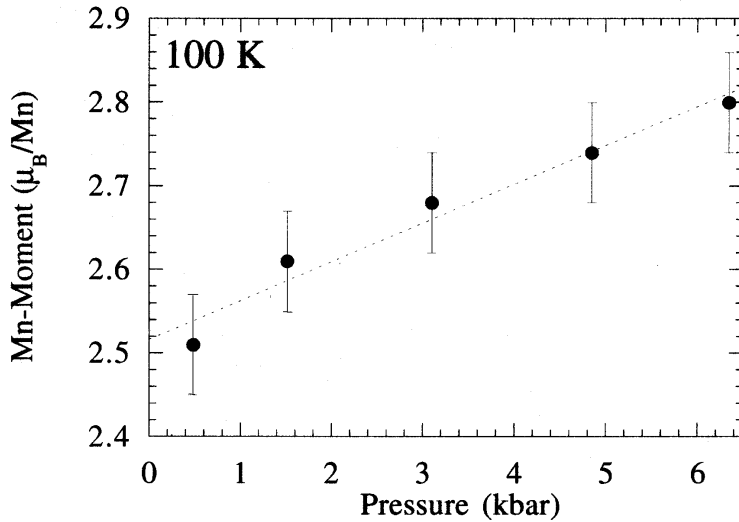


Fig. 11. Variation of the Mn moment with applied hydrostatic pressure at 100 K in $\text{La}_{1.2}\text{Sr}_{1.8}\text{Mn}_2\text{O}_7$.

4. The Manganite $\text{La}_{1.4}\text{Sr}_{1.6}\text{Mn}_2\text{O}_7$

(4a) Lattice Effects in $\text{La}_{1.4}\text{Sr}_{1.6}\text{Mn}_2\text{O}_7$

We turn our attention now to $\text{La}_{1.4}\text{Sr}_{1.6}\text{Mn}_2\text{O}_7$, a layered manganite with the same crystal structure as the previous composition but with a lower hole doping of $x = 0.3$. Kimura *et al.* (1996, 1997) have recently reported the observation of spin-polarised inter-layer conductivity and high CMR in the naturally layered materials $\text{La}_{2-2x}\text{Sr}_{1-2x}\text{Mn}_2\text{O}_7$, $x = 0.3$ ($10^4\%$ at 50 kOe and at 90 K). From magnetisation measurements they suggest that this layered manganite orders ferromagnetically (FM) along the c -axis at 90 K, but below 60 K an anomaly in the magnetisation suggests the development of canted interlayer antiferromagnetism (AF). This is in contrast to the ferromagnetic coupling observed in $\text{La}_{1.2}\text{Sr}_{1.8}\text{Mn}_2\text{O}_7$ discussed above. This AF coupling is believed to be responsible for the large tunneling magnetoresistance (TMR) observed in the c -axis transport at low temperatures (Kimura *et al.* 1996, 1997). Furthermore, these workers demonstrated that the magnetic coupling between perovskite layers may be manipulated with magnetic field or pressure; application of a magnetic field produces an increased interlayer conductivity while hydrostatic pressure decreases the conductivity along the c -axis and the ab -plane (Kimura *et al.* 1997). These behaviours have likewise been linked to a proposed AF structure.

Transport measurements on a small specimen from our crystal boule show a peak in both ρ_{ab} and ρ_c at $T_{\text{IM}} \sim 100$ K. This is consistent with the observations by Kimura *et al.* (1996, 1997) below 100 K on their $\text{La}_{1.4}\text{Sr}_{1.8}\text{Mn}_2\text{O}_7$ specimen. The chemical homogeneity of samples was investigated using high resolution X-ray diffraction as a response to the magnetic scattering which will be discussed in the next section.

It was found that in this compositional regime, there is strong evidence of a chemical phase separation (Argyriou *et al.* 1998). From the high resolution X-ray

diffraction studies two different $n = 2$ phases were identified. A major phase with lattice constants of $a = 3.86038(6)$ Å and $c = 20.2784(3)$, and a minor phase with $a = 3.8624(2)$ Å and $c = 20.2551(20)$ Å. The proportion of the minor phase is estimated to be $\sim 25\%$. The domain size of both phases is macroscopic (>1000 Å),

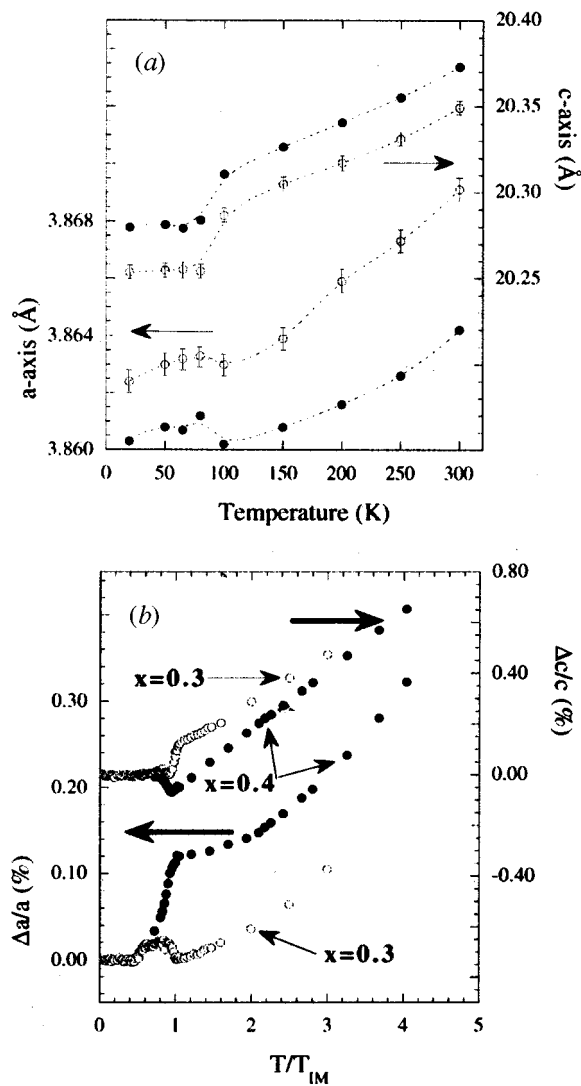


Fig. 12. Lattice parameters as a function of temperature for $\text{La}_{1.4}\text{Sr}_{1.6}\text{Mn}_2\text{O}_7$ ($x = 0.3$). (a) Lattice parameters for the major (open symbols) and minor (filled symbols) phases as a function of temperature as determined from synchrotron X-ray diffraction. (b) Lattice parameters from Rietveld analysis of neutron diffraction data from $x = 0.3$ (open symbols) and $x = 0.4$ (filled symbols). For the $x = 0.3$ sample, lattice parameters were determined from Rietveld analysis of diffraction data from the D20 spectrometer for $T < 150$ K and from SEPD between 20–300 K. For $x = 0.4$, the lattice parameters are taken from Hwang *et al.* (1995). Lattice parameters have been normalised to measurements at 5 K for $x = 0.3$ [$a = 3.86594(11)$ Å and $c = 20.29969(98)$ Å] and 20 K for $x = 0.4$ [$a = 3.86760(3)$ Å and $c = 20.06207(27)$ Å]. Error bars are smaller than the plot symbols. For $x = 0.4$, T_{IM} is 125 K.

as indicated by the FWHMs of the X-ray reflections: for the (2, 0, 0) reflection an angle $\sim 0.02^\circ$ and $\sim 0.03^\circ$ FWHM for major and minor phases respectively; for the (0, 0, 10) reflection an angle 0.04° and 0.06° FWHM again for major and minor phases respectively. At 20 K, the difference in lattice parameters (minor–major) is $\Delta a = 0.002 \text{ \AA}$ and $\Delta c = -0.026 \text{ \AA}$, much smaller than that reported by Battle *et al.* (1996) (e.g. $\Delta a = -0.008 \text{ \AA}$ and $\Delta c = 0.132 \text{ \AA}$ for $\text{LaSr}_2\text{Mn}_2\text{O}_7$). Such small differences are below the resolution of the instruments used in the neutron investigations ($\Delta d/d > 0.035$). Because the c/a ratio is expected to decrease with increasing Mn^{4+} concentration (due to the diminishing influence of the JT effect), these differences in lattice parameters for $x = 0.3$ are consistent with the majority component having a smaller value of dopant concentration x than the minority component. The temperature dependence of the lattice parameters of these two different phases is identical as indicated from the diffraction measurements (see Fig. 12).

The parallel variation of the lattice parameters in the majority and minority phases revealed by the X-ray study implies that even the ‘average’ structure probed by the neutrons qualitatively reflects the behaviour of the individual phases. As the neutron data measured on SEPD are more extensive in terms of both Q-range and temperatures measured than the X-ray measurements, refinements of these data will be used to discuss the structural evolution with temperature.

Similar to what has been observed in perovskites and in the $x = 0.4$ layered material, the $x = 0.3$ layered manganite demonstrates pronounced lattice effects (see Fig. 12) at T_{IM} . Above T_{IM} both a and c lattice parameters appear to decrease linearly with decreasing temperature. At T_{IM} , the c -axis contracts by 0.14% while the a -axis shows a slight expansion ($\sim 0.03\%$) between 100 and 50 K (see Fig. 12*b*). The exceedingly small magnitude of the a -axis expansion combined with the fact that the a -axis essentially tracks the development of magnetic order in the ab -plane (see next section) argues that the origin of this effect is purely magnetostrictive. The changes in lattice parameters at T_{IM} for $x = 0.3$ result in an overall volume contraction of $\sim 0.09\%$, (comparable to that of the $x = 0.4$ layered manganite and other manganite perovskites, see Radaelli *et al.* 1995; Mitchell *et al.* 1997; Caignaert *et al.* 1995). Interestingly, the *direction* of the lattice effects in this $x = 0.3$ is opposite to that of the $x = 0.4$ composition. In $x = 0.4$ materials the charge delocalisation is accompanied by an abrupt contraction of the a -axis by 0.16% and an expansion of the c -axis by $\sim 0.06\%$ (Mitchell *et al.* 1997). The temperature dependence of the $x = 0.4$ is also shown in Fig. 12*b* for comparison. It is not clear why the a -axis of the $x = 0.3$ sample changes by so little compared to $x = 0.4$, but the behaviour probably reflects a difference in the distribution of charge between these two compositions, which, as we shall discuss below, may result from a difference in their e_g orbital occupations.

The evolution with temperature of the three symmetry independent Mn–O bond lengths provides a microscopic view of the lattice response at T_{IM} . The largest effects are seen along the c -direction. Consistent with the temperature dependence of the a -axis, we find that the Mn–O(3) bond shows a monotonic decrease with temperature from 300 K down to T_{IM} . As shown in Fig. 13*a*, at T_{IM} Mn–O(3) (and hence the a -axis) expands slightly; in $x = 0.4$ it contracts, and considerably more so than in $x = 0.3$. The small anomaly between 100 and

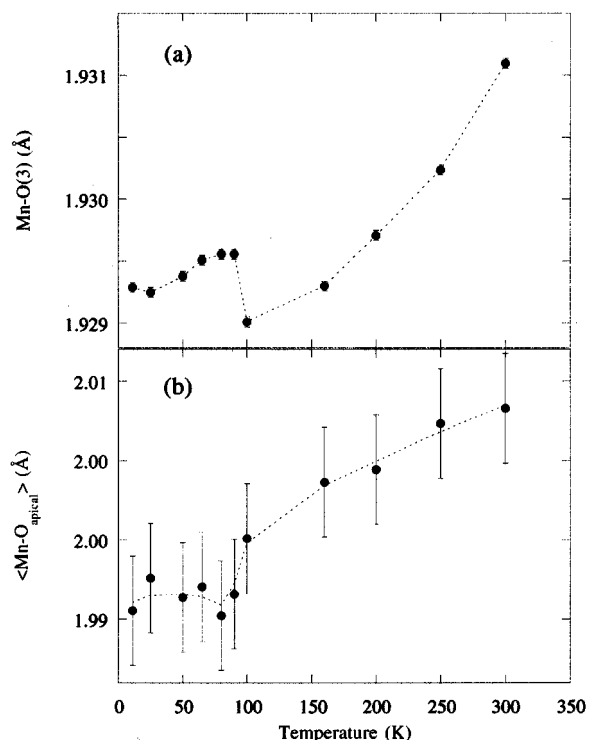


Fig. 13. Temperature dependence of (a) the Mn-O(3) bond lengths and (b) the $\langle \text{Mn-O}_{\text{apical}} \rangle$ bond, as given by $\frac{1}{2}[\text{Mn-O}(1)] + \frac{1}{2}[\text{Mn-O}(2)]$.

50 K on the a -axis results from changes in the Mn-O(3) bond associated with magnetostriction. Although not shown here, the a -axis varies linearly with the in-plane component of the Mn ordered moment, corroborating the assignment of this lattice parameter variation to magnetostriction.

The more significant changes occur along the c -axis at T_{IM} and can be understood in terms of the apical Mn-O bonds. Because determining the length of individual apical Mn-O bonds is complicated by the presence of two crystallographic phases in this sample, we look specifically at the average apical Mn-O bond, $\langle \text{Mn-O}_{\text{apical}} \rangle$ (Radaelli *et al.* 1995). As shown in Fig. 13b the average apical Mn-O bond contracts at T_{IM} by an amount that is approximately the same as the c -axis contraction. In $x = 0.4$, the c -axis expands at T_{C} by 0.06% (Hwang *et al.* 1995). The opposite behaviour of the lattice parameters between the $x = 0.3$ and $x = 0.4$ compositions also appears in the changes of the JT distortion of the MnO_6 octahedra below T_{IM} . In the $x = 0.4$ composition we reported that the octahedral distortion parameter, $D = \langle \text{Mn-O}_{\text{apical}} \rangle / \text{Mn-O}_{\text{equatorial}}$, *increases* by 0.6% at T_{IM} (Fig. 14). However, in this $x = 0.3$ material we find that it *decreases* by 0.3% at T_{IM} , suggesting that a more highly conductive electronic state is characterised by less distorted MnO_6 octahedra at this composition. This finding agrees with the recent pair distribution function analysis of neutron scattering data from a ceramic $x = 0.3$ sample reported by Louca *et al.* (1998).

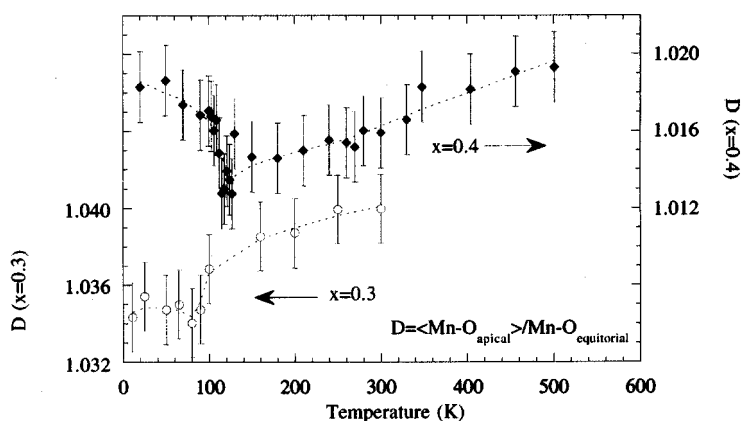


Fig. 14. Variation of the octahedral distortion parameter D as a function of temperature for $x = 0.3$ (open circles) and $x = 0.4$ (filled circles).

The same behaviour has also been noted for the manganite perovskites, for it has been widely shown that the octahedral distortion gets smaller—although it remains nonzero—in the metallic regime (Radaelli *et al.* 1995; Caignaert *et al.* 1995).

The different lattice effects observed in $x = 0.4$ and $x = 0.3$ cannot be accounted for purely by the change in the mean ionic radius of the rare-earth site cation. La and Sr are of similar ionic size, so between $x = 0.4$ and $x = 0.3$ the ionic radius changes by a mere 0.005 \AA . This indicates that the direction of the lattice effect at T_{IM} depends on the electronic doping, which in turn influences the character of the occupied orbitals on the Mn ion. In the $x = 0.4$ compound the contraction of the equatorial Mn–O(3) and the expansion of the apical Mn–O(2) bond at T_c is consistent with a charge transfer from in-plane $d_{x^2-y^2}$ orbitals above T_c to axially-directed $d_{3z^2-r^2}$ orbitals below T_c . Recent band structure calculations and ARPES measurements reported by Dessau *et al.* (1998) in single crystals of $x = 0.4$ material indicate that the $d_{x^2-y^2}$ orbital is slightly lower in energy than $d_{3z^2-r^2}$, but that these bands overlap substantially throughout the Brillouin zone. This near degeneracy of the orbitals indicates that charge transfer between the two orbital manifolds could be a reasonable response of the system to the coupled magnetic-electronic transition. In addition, Zhou *et al.* (1998) have suggested that in the $x = 0.4$ compound the application of pressure may result in a charge transfer from $d_{x^2-y^2}$ to $d_{3z^2-r^2}$ orbitals in the metallic state, perhaps resulting from this large overlap between e_g electronic states. In contrast, for the $x = 0.3$ sample the marked contraction of the c -axis on cooling through T_{IM} results directly from the contraction of the apical Mn–O bonds. This is consistent with a charge transfer from $d_{3z^2-r^2}$ orbitals to the planar $d_{x^2-y^2}$ orbital at T_{IM} , just the opposite of what is found in the $x = 0.4$ material. In this interpretation the analogy to Akimoto's A-type antiferromagnetic metal with conduction through $d_{x^2-y^2}$ orbitals in layers separated by unoccupied $d_{3z^2-r^2}$ orbitals is clear (Akimoto *et al.* 1998).

(4b) Magnetism in $\text{La}_{1.4}\text{Sr}_{1.6}\text{Mn}_2\text{O}_7$

The evolution of long range magnetic order in $\text{La}_{1.4}\text{Sr}_{1.6}\text{Mn}_2\text{O}_7$ was studied using neutron powder diffraction on D20. On cooling the sample, new magnetic

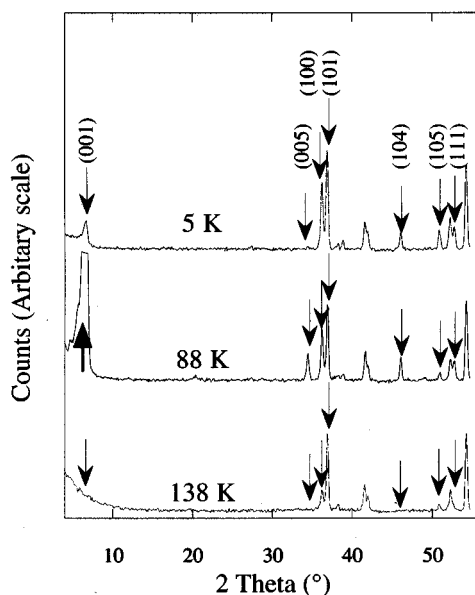


Fig. 15. Neutron powder diffraction data measured at various temperatures above and below T_{IM} from the $x = 0.3$ sample, on the D20 diffractometer ($\lambda = 2.41 \text{ \AA}$). Various FM and AF magnetic reflections are labelled.

reflections arise at T_{IM} indicative of a long-range AF state (see Fig. 15). Reflections such as the (001) and (005) arise below 100 K from AF stacking along the c -axis of FM perovskite bilayers with the Mn spins parallel to the ab -plane, μ_{ab}^{AF} . Also below 100 K the (100), (104) and (111) signal an AF ordering along the c -axis of FM bilayers with the Mn spins parallel to the c -axis, μ_c^{AF} . These arrangements are shown schematically in Figs 16*b* and 16*c*, while the crystal structure is shown in Fig. 16*a* for clarity. Inspection of the data revealed no signs of a FM stacking of FM in-plane moments, as seen in the $x = 0.4$ composition (Hwang *et al.* 1995). In both cases the observed antiferromagnetic reflections are consistent with a spin arrangement where Mn moments order ferromagnetically *within* perovskite bi-layers (*intra*-bilayer coupling is FM), but rotate by 180° in the adjacent layer, forming an antiferromagnetic *inter*-bilayer coupling (see Fig. 16*b*). The temperature dependence of the (111) and (001) reflections, characteristic of μ_c^{AF} and μ_{ab}^{AF} , is shown in Fig. 17. We note that the component of the AF moment in the ab -plane has a maximum in its temperature dependence at 80 K (see Fig. 17), indicating that the ordered moment rotates with cooling to form a tilted antiferromagnetic *inter*-bilayer coupling at low temperatures. This is the structure suggested by Kimura *et al.* (1997) from magnetisation measurements and by Heffner *et al.* (1998) from μSR measurements. A closer inspection of the diffraction data reveals additional intensity developing on the (101), (105) and (110) nuclear reflections below 75 K. This extra intensity is consistent with a ferromagnetic arrangement of Mn spins aligned along the c -axis, μ_c^{FM} (see Fig. 16*c*). The temperature dependence of the (105) reflections is also shown in Fig. 17. We emphasise that for the c -axis magnetic components, μ_c^{FM} and

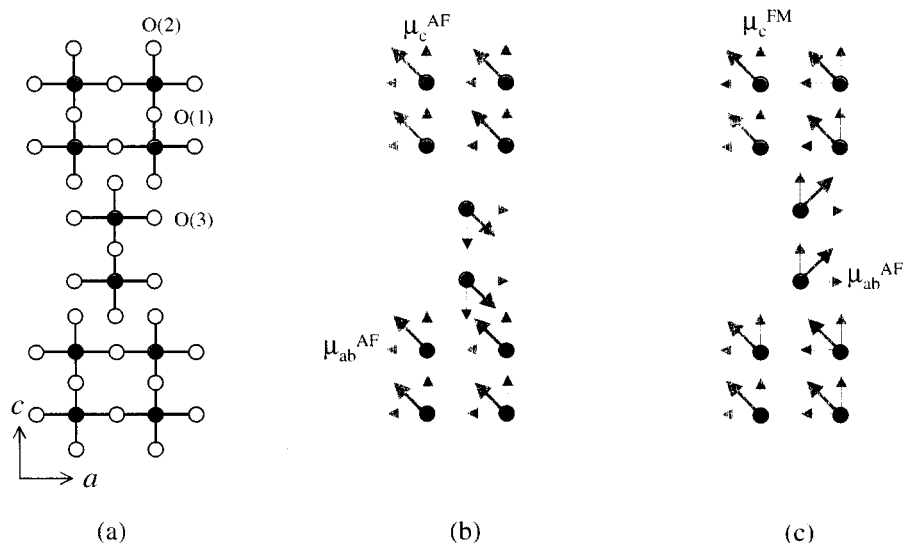


Fig. 16. (a) Crystal structure of $\text{La}_{2-2x}\text{Sr}_{1+2x}\text{Mn}_2\text{O}_7$ for $x = 3$. The three oxygen sites are shown, but not the La, Sr atoms. (b) Arrangement of Mn spins depicting the antiferromagnetic components μ_c^{AF} and μ_{ab}^{AF} (tilted antiferromagnet) and (c) the ferromagnetic component μ_c^{FM} in a canted ferromagnetic arrangement.

μ_c^{AF} , the perovskite bilayers remain ferromagnetically coupled; only the magnetic inter-bilayer coupling is different.

A determination of the low temperature magnetic structure was attempted using a number of single magnetic phase models with different combinations of AF and FM components. Clearly, the co-existence of AF and FM c -axis magnetic components is not compatible with spin canting. Refinement of the diffraction data using combinations of FM and AF perovskite layers, produced intensity under the observed magnetic reflections, but the magnitude of the calculated intensities agreed poorly with the data. Also models where Mn moments were constrained to be different between adjacent layers (ferrimagnetic model) did not improve the fit further and in some cases led to divergent refinements. Furthermore, the absence of any superlattice reflections in the data eliminated models that include an ordered arrangement of FM and AF coupled bilayers along the c -axis. We are thus led to conclude that the two magnetic components arise from distinct regions of the sample, each magnetically ordered over long length scales as indicated by resolution limited magnetic peak-widths. This conclusion agrees with the results of the synchrotron X-ray study discussed above under the assumption that distinct chemical phases have distinct magnetic structures associated with them.

The magnetic structures observed here (AF inter-bilayer coupling and FM inter-bilayer coupling) has not been observed in any *single-phase* composition of the $\text{La}_{2-2x}\text{Sr}_{1+2x}\text{Mn}_2\text{O}_7$ system. However, a layered manganite exhibiting a ferromagnetic structure with the Mn spins parallel to the c -axis is known for a doping level $x = 0.32$ (Kimura *et al.* 1996). Importantly, for $x > 0.35$, FM moments are aligned parallel to the ab -plane. This puts an upper concentration bound of $x = 0.32$ on any possible phase separation in our nominal $x = 0.3$

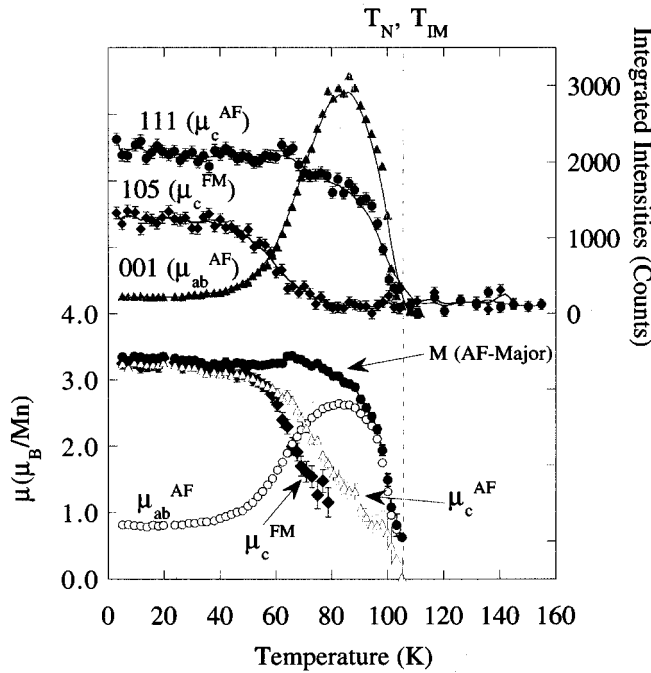


Fig. 17. Variation of intensities of the (111), (105) and (001) magnetic reflections as a function of temperature (upper panel). The (001) and (105) reflections represent directly the temperature dependence of the μ_{ab}^{AF} and μ_c^{FM} components respectively, while (111) represents a combination of μ_{ab}^{AF} and μ_c^{FM} components. The temperature dependence of the magnetic components μ_{ab}^{AF} , μ_c^{AF} and μ_c^{FM} and the total moment M in the AF majority phase based on Rietveld refinement of data measured on the D20 diffractometer are shown in the lower panel.

sample. Recent measurements on an $x = 0.4$ bilayer sample give an estimate of the inter-bilayer exchange in this compound as $J = 0.065$ eV (Rosenkrantz and Osborn 1998). It is not unreasonable to speculate that the sign of such a small exchange (FM versus AF) could depend sensitively on the chemical environment. For single-phase samples of $x = 0.32$, distinct ferromagnetic reflections appear at a T_c of ~ 125 K (Medarde and Mitchell 1998) much higher than the 75 K where c -axis FM coupling is first clearly observed in the present nominally $x = 0.3$ sample.

Good agreement with the neutron data at 5 K was found using models that included two distinct magnetic phases, consistent with the synchrotron X-ray results. In this analysis only one nuclear phase was included, as the phase separation behaviour was not resolved on D20. The assignment of the c -axis magnetic components is straightforward; the intensity of magnetic reflections arising from these c -axis components leads us to assign the μ_c^{AF} to the major phase and μ_c^{FM} to the minor phase. However, the assignment of the in-plane component is less clear. There are three possibilities: the in-plane AF component may be associated exclusively with the major phase (tilted AF structure); exclusively with the minor phase (canted FM structure); or divided between them (tilted AF structure+canted FM structure). Analysis of the data with μ_{ab}^{AF} assigned exclusively to either the AF-major or the FM-minor phases leads to a refined

total magnetic moment of $4.2 \mu_B/\text{Mn}$ at 80 K, substantially larger than the expected spin-only moment $3.7 \mu_B/\text{Mn}$ at this doping level. We thus take this as evidence that the in-plane component should be assigned to both major and minor phases.

With the available data we are not able to determine the relative contribution of the in-plane component in the two phases. To allow for this ambiguity, we have applied the following assumptions and/or constraints: (1) The saturation moment in both major and minor phases is the same ($\mu_{\text{sat}}^{\text{AF}} = \mu_{\text{sat}}^{\text{FM}}$). This assumption is valid because the small difference in the saturation moment due to composition ($\sim 0.02 \mu_B/\text{Mn}$) is much smaller than the experimental error in determining the size of the Mn moment ($\sim 0.3 \mu_B/\text{Mn}$). Application of this assumption allows us to determine the magnetic scale factor S at 5 K using the additional constraint of $S_{\text{AF}} + S_{\text{FM}} = S_{\text{crystallographic}}$. Here S_{AF} is the Rietveld scale factor for the tilted AF phase (see Fig. 5b), S_{FM} for the canted ferromagnetic phase (Fig. 5c) and $S_{\text{crystallographic}}$ the chemical or nuclear only scale factor. (2) The magnitude of the in-plane component was constrained to be the same for both major and minor phases [$\mu_{ab}^{\text{AF}}(\text{major}) = \mu_{ab}^{\text{AF}}(\text{minor})$]. This final constraint is arbitrary, but in the absence of additional information it is a simple, unbiased method of dividing the in-plane component between the two magnetic phases. Applying these constraints to the 5 K measurements, we obtain phase fractions of 62% (tilted AF phase) and 38% (canted FM phase). Given the difficulties of resolution, this result is in reasonable agreement with the ratio of major to minor chemical phases determined by the synchrotron X-ray measurements (75% and 25%). At 5 K the Rietveld analysis using these constraints yielded a saturation moment of $3.4(2) \mu_B/\text{Mn}$, in excellent agreement with the bulk magnetisation measurements of Kimura *et al.* (1997). Although we acknowledge that the model just described is not unique, it does represent a good fit to the available low temperature data and reproduces well the expected saturation moment at 5 K.

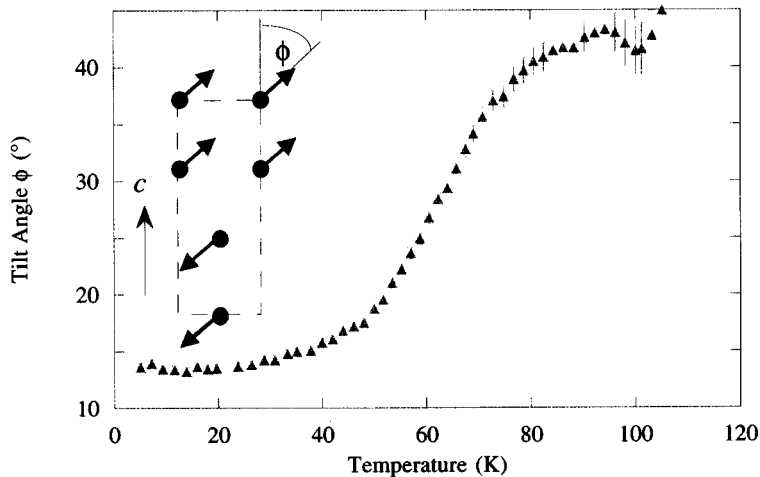


Fig. 18. Variation of the tilt angle ϕ as a function of temperature for the major phase in the nominal $x = 0.3$ sample.

The results of the analysis of the temperature dependent neutron diffraction data are shown in Fig. 17. For this analysis the magnetic scale factors for the major and minor magnetic phases were fixed to the value determined at 5 K. This constraint reflects the assumption that the magnetic phases are tied to distinct chemical phases whose fractions will not vary in this temperature regime. As in the 5 K refinement, the magnitude of the in-plane component for both phases was constrained to be the same. The analysis under these constraints shows that at 100 K Mn spins in the majority phase—which exhibits AF *inter*-bilayer and FM *intra*-bilayer coupling—order in a tilted arrangement with an angle $\phi d_{x^2-y^2} \sim 43^\circ$, from the *c*-axis. On cooling, Mn spins rotate towards the *c*-axis, reaching a final value of $\phi \sim 13^\circ$ at 5 K (see Fig. 18). We note that in this analysis the total magnetisation of the majority phase does not exceed the saturation moment at 80 K as occurred in a previously described model (see Fig. 7). The evolution of magnetic structure of the minor phase is similar to that of the major phase, except that no FM component is observed above 75 K. For the minor phase the data also suggest a transition from a canted to an almost co-linear ferromagnetic state at 5 K. However, the analysis of the data using this model indicates that, close to T_{IM} , the magnetic ordering in the minor phase is purely AF in the *ab*-plane. That both major and minor phases exhibit a similar temperature dependence of their lattice parameter suggest that the minor phases also undergo a similar rotation in the direction of the Mn moment as the majority phase. If this is correct, then there will be an FM inter-bilayer component in the minority phase above 75 K. As the ferromagnetic intensity appears superimposed on nuclear reflections, our sensitivity to this component is limited, particularly in a minority phase. Therefore at present we cannot rule out the possibility of a small ferromagnetic *c*-axis component (μ_c^{FM}) above 75 K in the minority phase.

5. Summary

Anisotropic systems such as $\text{La}_{2-2x}\text{Sr}_{1+2x}\text{Mn}_2\text{O}_7$ provide new opportunities to explore the relationship between magnetic, electronic, and structural transitions in the CMR manganites. Like the perovskite-based CMR materials, these layered compounds exhibit lattice effects correlated with magnetic ordering and charge delocalisation. We find structural behaviour consistent with a model in which hole doping leads to changes in the charge transfer on cooling through T_{IM} into $d_{3z^2-r^2}$ orbitals for $\text{La}_{1.2}\text{Sr}_{1.8}\text{Mn}_2\text{O}_7$ and into $d_{x^2-y^2}$ orbitals for $\text{La}_{1.4}\text{Sr}_{1.6}\text{Mn}_2\text{O}_7$. This demonstrates that the direction of lattice effects in layered materials is a sensitive function of charge and orbital degrees of freedom and implies a crossover between these two compositions. These variations in the orbital configuration of the Mn ion appear to correlate with changes in magnetic structure. In $\text{La}_{1.2}\text{Sr}_{1.8}\text{Mn}_2\text{O}_7$ we find a ferromagnetic structure with Mn spins lying in the *ab*-plane. However, we demonstrate that this simple picture is not a sufficient description as the competition between super and double exchange results in a canting of spins between adjacent MnO_2 sheets. In $\text{La}_{1.4}\text{Sr}_{1.6}\text{Mn}_2\text{O}_7$ we observe a more complex behaviour. Here two $n = 2$ phases show considerable similarity in terms of both composition ($\delta x \sim 0.02$) and lattice effects at T_{IM} . The lattice parameters of these two phases track one another in parallel with temperature—including the anomaly through the magnetic transition—indicating a similar charge–spin–lattice coupling. We find that the main difference between these two phases lies in

their magnetic structure, which exhibits a clear temperature dependence. At 5 K the majority phase exhibits AF inter-bilayer coupling, as suggested by other workers (Kimura *et al.* 1997; Heffner *et al.* 1998), while the minority phase shows FM inter-bilayer coupling. It is interesting to note that despite the different *inter*-bilayer coupling, the lattice parameters of both phases parallel one another as a function of temperature. This suggests that the spin–lattice interaction is largely confined to the perovskite blocks and that inter-bilayer spin–lattice coupling is considerably weaker. Both X-ray and neutron results imply that the minority phase has a greater hole concentration than the majority phase, suggesting that hole rich compositions favour FM inter-bilayer coupling. This is consistent with the broader picture of the (La, Sr)₃Mn₂O₇ phase diagram (Medarde and Mitchell 1998).

Acknowledgments

We thank R. B. von Dreele for allowing some preliminary powder diffraction measurements on La_{1.4}Sr_{1.6}Mn₂O₇ on the HIPD spectrometer at the Manuel Lujan Jr Neutron Scattering Centre, Los Alamos National Laboratory. Preliminary neutron scattering data from single crystals of $x = 0.3$ were also measured on SCD at the Lujan centre. We also thank R. Heffner and K. Gray for making available preprints of their work on these materials, and S. Short and O. Chmaissem for their assistance in the high pressure experiments. This work was supported by the US Department of Energy, Basic Energy Sciences-Materials Sciences under contract W-7405-ENG-36 (DNA, HNB), W-31-109-ENG-38 (JFM, JDJ) and DE-AC02-98CH10886 (DEC), and UC DRD grant No. STB-UC:97-240 (HNB). DNA also thanks the Institut Laue–Langevin for financial support, and the organising committee of the International Workshop on CMR, GMR, High T_c and Structural Determination by Electron, X-ray and Neutron Diffraction, for financial support and their generous hospitality.

References

- Akimoto, T., Maruyama, Y., Moritomo, Y., Nakamura, A., Hirota, K., Ohoyama, K., and Ohashi, M. (1998). *Phys. Rev. B* **57**, 5594.
- Archibald, W., Zhou, J.-S., and Goodenough, J. B. (1996). *Phys. Rev. B* **53**, 14445.
- Argyriou, D. N., Mitchell, J. F., Potter, C. D., Bader, S. D., Kleb, R., and Jorgensen, J. D. (1997a). *Phys. Rev. B* **55**, 11965–8.
- Argyriou, D. N., Mitchell, J. F., Goodenough, J. B., Chmaissem, O., Short, S., and Jorgensen, J. D. (1997b). *Phys. Rev. Lett.* **78**, 1568–71.
- Argyriou, D. N., Mitchell, J. F., Radaelli, P. G., Bordallo, H. N., Cox, D. E., Medarde, M., and Jorgensen, J. D. (1999). *Phys. Rev. B* **59**, 8695–702.
- Battle, P. D., Green, M. A., Laskey, N. S., Millburn, J. E., Rosseinsky, M. J., Sullivan, S. P., and Vente, J. F. (1996). *Chem. Commun.* 767–8.
- Billinge, S. J. L., Difrancesco, R. G., Kwei, G. H., Neumeier, J. J., and Thompson, J. D. (1996). *Phys. Rev. Lett.* **77**, 515.
- Booth, C. H., Bridges, F., Kwei, G. H., Lawrence, J. M., Cornelius, A. L., and Neumeier, J. J. (1998). *Phys. Rev. Lett.* **80**, 853–6.
- Caignaert, V., Maignan, A., and Raveau, B. (1995). *Solid State Commun.* **95**, 357.
- Dessau, D. S., Saitoh, T., Park, C. H., Shen, Z. X., Vilella, P., Hamada, N., Moritomo, Y., and Tokura, Y. (1998). *Phys. Rev. Lett.* **81**, 192–5.
- Fontcuberta, J., Martinez, B., Seffar, A., Pinol, S., Garciamunoz, J. L., and Obradors, X. (1996). *Phys. Rev. Lett.* **76**, 1122–5.
- Goodenough, J. B. (1963). 'Magnetism and the Chemical Bond' (Wiley: New York).

- Goodenough, J. B. (1972). In 'Progress in Solid State Chemistry' (Ed. H. Reiss), Vol. 5, p. 145 (Pergamon: Oxford).
- Heffner, R. H., MacLaughlin, D. E., Nieuwenhuys, G. J., Kimura, T., Luke, G. M., Tokura, Y., and Uemura, Y. J. (1998). *Phys. Rev. Lett.* **81**, 1706.
- Hirota, K., Moritomo, Y., Fujioka, H., Kubota, M., Yoshizawa, H., and Endoh, Y. (1998). *J. Phys. Soc. Jpn* **67**, 3380.
- Hwang, H. Y., Cheong, S.-W., Radaelli, P. G., Marezio, M., and Batlogg, B. (1995). *Phys. Rev. Lett.* **75**, 914.
- Jonker, G. H., and Santen, J. H. V. (1950). *Physica* **16**, 337.
- Jorgensen, J.-E., Jorgensen, J. D., Batlogg, B., Remeika, J. P., and Axe, J. D. (1986). *Phys. Rev. B* **33**, 4793.
- Kim, K. H., Gu, J. Y., Choi, H. S., Park, G. W., and Noh, T. W. (1996). *Phys. Rev. Lett.* **77**, 1877–80.
- Kimura, T., Asamitsu, A., Tomioka, Y., and Tokura, Y. (1997). *Phys. Rev. Lett.* **79**, 3720–3.
- Kimura, T., Kumai, R., Tokura, Y., Li, J. G., and Matsui, Y. (1998). *Phys. Rev. B* **58**, 11081.
- Kimura, T., Tomioka, Y., Kuwahara, H., Asamitsu, A., Tamura, M., and Tokura, Y. (1996). *Science* **274**, 1698–701.
- Li, Q. A., Grey, K. E., and Mitchell, J. F. (1998). *Phys. Rev. B*, submitted.
- Louca, D., Kwei, G. H., and Mitchell, J. F. (1998). *Phys. Rev. Lett.* **80**, 3811.
- Medarde, M., and Mitchell, J. F. (1998). personal communication
- Millis, A. J., Littlewood, P. B., and Shraiman, B. I. (1995). *Phys. Rev. Lett.* **74**, 5144–7.
- Mitchell, J. F., Argyriou, D. N., Jorgensen, J. D., Hinks, D. G., Potter, C. D., and Bader, S. D. (1997). *Phys. Rev. B* **55**, 63–6.
- Mitchell, J. F., Milburn, J. E., Medarde, M., Jorgensen, J. D., and Argyriou, D. N. (1998). *J. App. Phys.*, in press.
- Moritomo, Y., Asamitsu, A., Kuwahara, H., and Tokura, Y. (1996). *Nature* **380**, 141.
- Osborn, R., Rosenkranz, S., Argyriou, D. N., Vasiliu-Doloc, L., Lynn, J. W., Sinha, S. K., Mitchell, J. F., and Grey, K. E. (1999). *Phys. Rev. Lett.* **81**, 3964–7.
- Radaelli, P. G., Cox, D. E., Marezio, M., Cheong, S.-W., Schiffer, P. E., and Ramirez, A. P. (1995). *Phys. Rev. Lett.* **75**, 4488.
- Radaelli, P. G., Marezio, M., Hwang, H. Y., Cheong, S. W., and Batlogg, B. (1996). *Phys. Rev. B* **54**, 8992–5.
- Roder, H., Zang, J., and Bishop, A. R. (1996). *Phys. Rev. Lett.* **76**, 1356–9.
- Rosenkranz, S., and Osborn, R. (1998). personal communication.
- Torrance, J. B., Lacorre, P., and Nazzari, A. I. (1992). *Phys. Rev. B* **45**, 8209.
- Wollan, E. O., and Koehler, W. C. (1955). *Phys. Rev.* **100**, 545.
- Zener, C. (1951). *Phys. Rev.* **51**, 403.
- Zhao, G.-M., Conder, K., Keller, H., and Müller, K. A. (1996). *Nature* **381**, 676.
- Zhao, Y., Weidner, D. J., Parise, J. B., and Cox, D. E. (1993). *Phys. Earth Planet. Inter.* **76**, 17.
- Zhou, J.-S., Goodenough, J. B., and Mitchell, J. F. (1998). *Phys. Rev. B* **58**, R579.